

Energy Advances

Accepted Manuscript

This article can be cited before page numbers have been issued, to do this please use: S. Orozco-Barrera, J. A. Lirio Piñar, C. Kök, G. R. Iglesias, A. Delgado, V. Presser and S. Ahualli, *Energy Adv.*, 2026, DOI: 10.1039/D6YA00009F.



This is an Accepted Manuscript, which has been through the Royal Society of Chemistry peer review process and has been accepted for publication.

Accepted Manuscripts are published online shortly after acceptance, before technical editing, formatting and proof reading. Using this free service, authors can make their results available to the community, in citable form, before we publish the edited article. We will replace this Accepted Manuscript with the edited and formatted Advance Article as soon as it is available.

You can find more information about Accepted Manuscripts in the [Information for Authors](#).

Please note that technical editing may introduce minor changes to the text and/or graphics, which may alter content. The journal's standard [Terms & Conditions](#) and the [Ethical guidelines](#) still apply. In no event shall the Royal Society of Chemistry be held responsible for any errors or omissions in this Accepted Manuscript or any consequences arising from the use of any information it contains.

View Article Online
DOI: 10.1039/D6YA00009F

Lithium-ion electrosorption on lithium manganese oxide soft and bare electrodes

S. Orozco-Barrera^{1†}, J. A. Lirio Piñar^{1†}, C. Kök^{2,3}, G. R. Iglesias^{1,4},
A. V. Delgado¹, V. Presser^{2,3,5*}, S. Ahualli^{1*}

- ¹ Department of Applied Physics, School of Sciences, University of Granada, 18071 Granada, Spain.
- ² INM - Leibniz Institute for New Materials, Campus D2 2, 66123 Saarbrücken, Germany.
- ³ Department of Materials Science & Engineering, Saarland University, Campus D2 2, 66123 Saarbrücken, Germany.
- ⁴ NanoMag Lab. Department of Applied Physics. Edificio I+D Josefina Castro, University of Granada, Spain.
- ⁵ saarene - Saarland Center for Energy Materials and Sustainability, Campus C4 2, 66123 Saarbrücken, Germany.

***Corresponding authors:**

V. Presser: Volker.presser@leibniz-inm.de

S. Ahualli: sahualli@ugr.es

† These authors contributed equally to this work



Abstract

View Article Online
DOI: 10.1039/D6YA00009F

Lithium is a critical resource for high-energy batteries and emerging energy storage technologies. Conventional extraction methods, such as solar evaporation of brines, are energy-intensive and environmentally harmful, highlighting the need for sustainable alternatives. Here, we present an electrochemical electrosorption strategy for selective lithium recovery using a hybrid intercalation-based electrochemical cell that exploits the unique properties of lithium manganese oxide (LMO). Unlike traditional carbon-based electrodes, LMO features a spinel crystal structure that enables reversible Li^+ intercalation under controlled potentials, providing intrinsic ion selectivity. To improve durability and performance, the LMO electrode was functionalized with the anionic polyelectrolyte poly(sodium 4-styrenesulfonate) (PSS). At the same time, the activated carbon counter-electrode was coated with the cationic polyelectrolyte poly(diallyldimethylammonium chloride) (PDADMAC). Experiments in single-salt (LiCl) and mixed-salt (LiCl + NaCl) systems, including highly asymmetric brines, reveal that Li^+ uptake strongly depends on the applied cell voltage, reaching values above 40 mg/g at 1.2 V. The PSS coating mitigates Mn dissolution and alters desorption dynamics, favoring Na^+ release while enhancing Li^+ retention. These results demonstrate the potential of LMO-based hybrid electrodes for energy-efficient lithium recovery from complex saline environments.

Keywords:

electrosorption; lithium-ion recovery; LMO; mixed solutions; polyelectrolyte soft electrode



1. Introduction

Lithium is a crucial element in industry, particularly notable for its significance in the production of high-energy-density rechargeable batteries and other electronic devices ¹⁻⁴.

The demand for lithium has grown exponentially in recent decades, driven by the rise of electromobility and the increasing need for renewable energy storage. The primary sources of lithium are brines found in salt flats ⁵⁻⁷ and minerals such as spodumene ⁸. The most significant lithium-rich brine deposits are located in the region known as the lithium triangle in South America, which encompasses Argentina, Bolivia, and Chile. The most common conventional extraction process is based on solar evaporation, a technique that involves the evaporation of large volumes of water to concentrate the salts and extract the lithium ⁹⁻¹¹. In these large-scale operations, the high aqueous solubility of lithium chloride, 830.5 g/L at 20 °C ¹², allows lithium cations to remain in solution while other salts precipitate. Once the brine is sufficiently concentrated, chemical precipitation is induced using carbonate precursors, such as adding Na₂CO₃ to precipitate Li₂CO₃, taking advantage of its much lower solubility limit ¹³.

Despite its widespread use, this carbonate-based recovery is ineffective for dilute sources, as the solubility limit of Li₂CO₃ cannot be reached without prior and extensive concentration of LiCl, often requiring 12 to 24 months to complete ¹⁴. Furthermore, this method is associated with significant environmental challenges, including intensive water usage in arid regions and the generation of saline waste, which can have detrimental effects on local biodiversity ^{9, 15}.

Electrochemical methods emerge as a promising technology for more efficient and sustainable lithium extraction from low-concentration aqueous streams in a matter of hours ¹⁶⁻¹⁸. As an example, capacitive deionization, employing ion electrosorption as the ion



removal mechanism¹⁹, may enable the selective recovery of ions from aqueous solutions or brines²⁰⁻²². Compared to conventional methods, capacitive deionization can operate more efficiently at a smaller scale. This makes it a competitive option for lithium recovery, particularly in cases where traditional techniques are either ineffective or harmful to the environment²³⁻²⁶. However, without proper functionalization of the electrodes, this technique is not efficient in selectively separating monovalent cations such as Na⁺ and Li⁺. In this context, hybrid electrochemical ion separation cells, where one of the electrodes is constructed with intercalation materials, provide a more accurate description of the system studied here, as ion trapping occurs via redox intercalation rather than double-layer adsorption²⁷.

Using LiMn₂O₄ (LMO) as the primary active material provides a unique ability to selectively intercalate Li⁺.^{24, 28-30} LMO is a compound that presents a spinel-like crystal structure, which facilitates efficient ion mobility and enables high reversibility in the intercalation and deintercalation of Li⁺. This property is crucial to maintain the structural integrity of the material over multiple charge-discharge cycles³¹. Also, its relatively low production cost and low environmental impact compared to other materials, which reinforces its feasibility for electrode synthesis, make LMO suitable for electrochemical systems.³²

A key aspect of this process is how the active electrode material participates in the transfer of electrons during the redox reaction (**Eq. 1**):



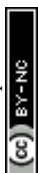
where x represents the fraction of lithium intercalated or deintercalated during charging or discharging. In this reaction, Li⁺ enters the LMO lattice and occupies specific sites in the crystal structure.



Unlike LMO's smaller surface area (<2 m²/g), activated carbons are known for their large specific surface area. Consequently, its sorption performance depends on the electrode composition and current operating conditions³³⁻³⁵. Recent studies have demonstrated that the coating of carbon electrodes with polyelectrolytes can substantially augment their ion removal capacity and overall desalination performance³⁶⁻³⁹. This enhancement is attributed to the promotion of counterion transport and the suppression of co-ion release, resulting in improved charge efficiency and stability^{36-38, 40-43}.

This study focuses on elucidating the influence of polyelectrolyte coating on the performance of hybrid electrochemical ion separation cells employing LMO as the active electrode material. Poly(sodium 4-styrenesulfonate) PSS is utilized as an anionic coating for the LMO electrode, while poly(diallyldimethylammonium chloride) (PDADMAC) is employed as a cationic coating for the AC counter-electrode. The selection of these polymers was predicated on their water-solubility, commercial availability, and established role in the literature concerning the enhancement of charge efficiency and electrode stability in capacitive deionization systems^{36, 44}. PSS has been reported to enhance lithium-ion transport⁴⁴⁻⁴⁷ and to mitigate the detrimental effects of the Jahn–Teller distortion, which can lead to Mn dissolution during electrochemical cycling^{48, 49}. This modification is expected to enhance the material's durability and maintain its lithium selectivity over prolonged operation. PDADMAC has demonstrated benefits in stabilizing and improving the capacitive performance of carbon electrodes³⁹. However, the influence of such coatings on intercalation-type electrodes, such as LMO, has not yet been systematically explored.

A series of systematic experiments was conducted in which key operational parameters, such as the applied voltage, LMO-to-AC mixing ratio, and electrode connection mode during the discharge step, were varied. The goal was to assess how these variations influence the



selective uptake and release of Li^+ and Na^+ ions. A distinctive feature of this study is the real-time visualization of the desalination cycles through conductivity monitoring, which enables in situ evaluation of ion-removal dynamics and kinetics. This approach provides novel insights into the role of polymer coatings in enhancing both the selectivity and the structural stability of LMO-based electrodes for Li^+ recovery from mixed brines^{37, 39, 41}.

2. Experimental

2.1. Materials

LiCl (99.98 % purity, Sigma Aldrich) and NaCl (99.73 % purity, Fisher Chemicals) solutions were prepared in Milli-Q water (Milli-Q Academic, Millipore). LiMn_2O_4 (>98 % purity, Sigma Aldrich), YP-80F activated carbon (AC) (supplied by Kuraray), and carbon black (>99 % purity, Thermo Fisher) were used as materials in the preparation of the electrodes. Polydiallyldimethylammonium chloride (PDADMAC) (average molecular weight above 100,000, Sigma Aldrich) and PSS (average molecular weight of 70,000, Sigma Aldrich) were used as cationic and anionic polyelectrolytes, respectively, to coat the electrodes where appropriate. In addition, a commercial anion exchange membrane (AMX, Tokuyama) from Neosepta, with a thickness of 140 μm , was placed in front of the AC electrode.

2.2. Particle characterization

The particle morphology was obtained from high-resolution electron microscope (Thermo Fisher Scientific TALOS F200X microscope) pictures. The particle size distributions in water were determined by dynamic light scattering (Malvern Zeta Sizer Nano-ZS, Malvern Pananalytical). Nitrogen sorption measurements at $-196\text{ }^\circ\text{C}$ were performed using a Quadrasorb IQ system (formerly Quantachrome; now Anton Paar) after degassing the



samples under vacuum at 100 °C for 12 h. The specific surface area was calculated using the Brunauer-Emmett-Teller method⁵⁰⁻⁵². Quenched solid density functional theory was used to calculate the pore size distribution, assuming slit-shaped pores.

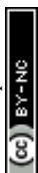
The structural properties of the particles were evaluated by powder X-ray diffraction using a Bruker D8 Discover diffractometer equipped with a Pilatus3R 100K-A detector. The experiments were conducted at 25 °C, employing Cu K α radiation ($\lambda = 1.5406 \text{ \AA}$) with an operating voltage of 50 kV and a current of 1 mA. Data were collected over a 2θ range of 5° to 85°, with a step size of 0.02° and a counting time of 40 s per step, and compared with diffractograms generated by the PowderCell 2.4 software (developed by the Federal Institute for Materials Research and Testing).

Chemical analysis of the materials was performed by Fourier-Transform infrared spectroscopy in an FT/IR-6200 spectrometer, JASCO, with a resolution of 0.25 cm⁻¹.

2.3. Electrode preparation

The electrochemical cell employed in this study consists of two flat electrodes arranged in a parallel-plate configuration. The working electrode was made of LMO or its PSS-coated counterpart (LMO-soft), while the counter-electrode was prepared from AC or PDADMAC-functionalized AC (AC-soft). Both electrodes were assembled on graphite current collectors and separated by a 400 μm insulating spacer, with an anion-exchange membrane (AMX) positioned adjacent to the carbon electrode.

For the preparation of the active electrode material, 0.23 g of active material (a mixture of AC and LMO, hereafter referred as AC:LMO) and carbon black powder mixture (95:5 ratio by mass) was added to 0.77 g of a 33 g/L suspension of poly-vinylidene-fluoride (PVDF), manufactured by Arkema as Kynar HSV 900, with molecular weight approximately 1,000,000



in 1-methyl 2-pyrrolidone (Sigma Aldrich). The AC:LMO mass/mass ratios employed in this study are 0:100 (hereafter referred to as LMO), 20:80, 40:60, and 60:40. The suspension was magnetically stirred until a homogeneous slurry was obtained and spread on the surface of a graphite plate (Mersen) serving as the current collector. The electrode was dried overnight at 70 °C, yielding 0.04 ± 0.01 g of active material with a characteristic bluish-gray appearance, as shown in *Supplementary Information, Figure S1A*.

Prior to the assembly of the LMO electrode in a measuring cell, it was subjected to a pre-treatment process to ensure the release of Li^+ from the LMO structure itself, thus allowing the electrode to trap-release Li^+ during sorption-desorption measurements. For this, the electrode was immersed in a 30 mM LiCl solution, and 1 V was applied for 120 min²⁸. After this process, the electrode becomes reddish, which is characteristic of the delithiated LMO (*Supplementary Information, Figure S1B*).

The polymeric coating of the LMO electrode was carried out by immersing the already formed electrode in a stirred 200 mM aqueous solution of PSS overnight. After this stage, the electrode was rinsed thrice with deionized water (Milli-Q) and dried at room temperature⁵³.

For the coating of the AC counter-electrode, the carbon powder was dispersed in 200 mM PDADMAC solution, stirred for 12 h, centrifuged, and redispersed in water at least three times or as needed for complete removal of the non-adsorbed polyelectrolyte. Finally, the carbon particles were dried at 65 °C and used for the preparation of the electrode as described above⁵⁴.

The desalination cell was described in detail in⁴⁰. The active area of the electrodes is 50 cm². The LMO (or LMO-soft) electrode is placed facing the AC (or AC-soft) counter-electrode,



separated by a 400 μm mesh insulating spacer. The AMX membrane was always placed next to the latter electrode.

View Article Online
DOI: 10.1039/D6YA00009F

2.4. Electrochemical Li^+ recovery

The experimental method described in Ref. ³⁶ was followed to perform electrochemical Li^+ recovery. Briefly, in the absorption step, the LMO electrode was set at -0.4 V, -0.9 V, or -1.2 V with respect to the AC-soft electrode by means of an Ivium-Stat potentiostat (Ivium Technologies) in a two-electrode configuration. Because of this setup without a standard reference electrode, it is important to clarify that the reported voltage values throughout this work represent the total cell voltage (i.e., the potential difference applied between the LMO working electrode and the AC counter electrode). For desorption, an opposite cell voltage (reverse voltage or RV) was applied to reach the potential for controlled deintercalation of the ions from the LMO structure. The electrolyte solutions investigated were LiCl 10 mM, NaCl 5 mM + LiCl 5 mM, and NaCl 9.5 mM + LiCl 0.5 mM. The flow rate was 0.7 mL/s, and each cycle duration was 10 min.

2.5. Determinations of the ionic composition of the solutions

A follow-up of the ion uptake and release processes was carried out by in-line measurements of electrical conductivity using a 529670-conductivity probe connected to a Leybold 524D10 Cassy Lab interface (Leybold). To evaluate the concentrations of individual ions, two types of measurements were conducted. Ion chromatography was employed for online determinations, whereby 2 mL samples were taken at various times during the cycle to identify the type and concentration of the ionic species of interest at each step of the



process. The analysis of the samples was performed with a 940 Professional IC Vario ion chromatograph (Metrohm).

Real-time measurements were performed to determine ionic concentrations of the target species, lithium, and sodium, at the outlet of the desalination cell⁵⁵. This was carried out by inductively coupled plasma optical emission spectroscopy (ICP-OES) using a SPECTRO ARCOS ICP-OES analyzer (Spectro Ametek) with a flow rate of 1 mL/min.

3. Results and discussion

3.1. Particles characterization

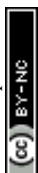
Figure 1C-E shows electron micrographs of the LMO, AC, and carbon black samples. The appearance of the former is plate-like with an average size of 45 ± 14 nm. The AC particles exhibit pores and have a size of $2.9\ \mu\text{m}$ (d_{50}), while the carbon black particles were about 32 ± 15 nm in size. The nitrogen adsorption isotherms (*Supplementary Information, Figure S2*) demonstrate a very high specific surface area for AC ($2029\ \text{m}^2/\text{g}$) as compared to the other samples ($15\ \text{m}^2/\text{g}$ for LMO and $56\ \text{m}^2/\text{g}$ for carbon black).

X-ray diffractograms are plotted in **Figure 1F**. As can be observed, the peaks obtained for LMO coincide with those in the theoretical diffractogram considering a unit cell with the space group $Fd3m$ and $8.2476\ \text{\AA}$ cell size, with Li^+ , $\text{Mn}^{3+}/\text{Mn}^{4+}$, and O^{2-} ions occupying Wyckoff positions 8a, 16d, and 32e, respectively (**Figure 1A,B**)^{56, 57}. The diffractograms obtained for LMO with and without PSS coating are practically identical, indicating that the crystal structure remains unaffected by the functionalization with the polyelectrolyte. This is advantageous due to the selective properties of LMO towards Li^+ , which are derived from its spinel-like structure^{24, 28-31}.



As evident in the diffractogram of activated carbon AC (*Supplementary Information, Figure S3*), the absence of peaks indicates that it is a non-crystalline, amorphous solid⁵⁶. A broad peak can be observed at approximately $2\theta = 23.5^\circ$, which can be attributed to the short-range order of the hexagonal arrangement of the carbon atoms, which is analogous to that observed in graphite⁵⁷. The presence of partially ordered mesopores can be inferred from the peak that appears at small angles, $2\theta < 5^\circ$ ⁵⁸. This appears to be attenuated by the PDADMAC coating, which may be indicative of pore occlusion resulting from polyelectrolyte deposition⁵⁹⁻⁶¹.

Infrared spectra were obtained for LMO and AC, and their functionalized variants, as displayed in **Figure 1G** and *Supplementary Information, Figure S4*. As demonstrated in **Figure 1G**, LMO is characterized by a series of pronounced peaks, which are indicative of two distinct vibrational modes of the manganese-oxygen bonds appearing at $500-580\text{ cm}^{-1}$ and $620-650\text{ cm}^{-1}$, respectively⁶². Furthermore, the spectrum also exhibits traces of environmental water and carbon dioxide. Conversely, PSS-functionalized LMO exhibited the bands indicative of PSS polyelectrolyte⁶³. For instance, the following vibrational modes have been identified: (C-H) sp^3 (aliphatic) stretches at $2850-2960\text{ cm}^{-1}$ ^{63, 64}; aromatic C=C stretches at $1500-1600\text{ cm}^{-1}$ ⁶⁵, symmetric ($1180-1250\text{ cm}^{-1}$) and asymmetric ($1030-1040\text{ cm}^{-1}$) stretches of the sulfonate groups^{66, 67}. Furthermore, a peak at approximately 1130 cm^{-1} was identified in the functionalized LMO spectrum, which is most likely attributable to vibrations of the sulfonate group of PSS, displaced by electrostatic or coordinative interactions with the LMO surface^{68, 69}. These results confirm the presence of PSS on LMO particles, as well as the interaction of the polyelectrolyte with the surface of the particles. The results for the AC and its PDADMAC functionalization are displayed in *Supplementary Information, Figure S4*. The analysis of the spectra revealed that both substances exhibit



peaks at 1000-1100 cm^{-1} , which correspond to the C-O stretching modes of surface oxygenated groups ⁷⁰. Additionally, the spectra demonstrate peaks at 1600-1620 cm^{-1} , which correspond to the C=C stretching of the graphitic skeleton of the AC ⁷¹. Further analysis indicates peaks at 2850-2920 cm^{-1} , which are indicative of aliphatic C-H stretching and suggest that the material is not fully graphitized ⁷². Finally, the spectra show peaks at 3200-3600 cm^{-1} , which correspond to medium water and hydroxyl groups ⁷³. Additionally, traces of environmental carbon dioxide (CO_2) were detected. Other bands observed in AC-soft can be ascribed to the presence of PDADMAC, as reported in ⁷⁴. In particular, bands at 950-1050 cm^{-1} C-N⁺ vibrations, and at 1380-1400 cm^{-1} methyl symmetric bending of the CH_3 group ^{75, 76}. A peak at 1620-1640 cm^{-1} is indicative of water absorbed on a hydrophilic cationic polymer ⁷⁷.

3.2. Influence of the applied cell voltage on electrosorption

Before evaluating the influence of the applied cell voltage, it is important to recall that the extraction process of Li^+ ions from LMO requires activation of the material by applying a positive voltage to overcome the lithium diffusion barrier ^{78, 79}. It has been reported that for undoped LMO, the barrier is approximately 0.35 eV, and it is presumed to be higher at the material surface ⁸⁰. Based on experimental cyclic voltammetry data, a cell voltage of 0.9 V is sufficient for activation, highlighting the importance of precise voltage control to enhance sorption efficiency ^{81, 82}.

To examine how the cell voltage affects electrosorption once the activation threshold is reached, experiments were conducted at three cell voltages: 0.4 V, 0.9 V, and 1.2 V. To evaluate the influence of the applied voltage on electrosorption, two characteristic



parameters were considered: the specific adsorption capacity (SAC) and the charge efficiency (ε). The SAC is defined as (Eq. 2)

$$SAC = \frac{\int_{\text{half cycle}} [c_{out} - c_{in}] \phi_v dt}{m}, \quad (2)$$

where c_{out} (c_{in}) is the outlet (inlet) electrolyte concentration, ϕ_v is the pumping flow rate, and m is the mass of the active material on both electrodes. Another characteristic parameter is the charge efficiency, or the ratio between the charge of the removed ions and the charge of the transferred electronic charge, given by

$$\varepsilon = \frac{\int_{\text{half cycle}} [c_{out} - c_{in}] \phi_v F dt}{\int_{\text{half cycle}} I dt}, \quad (3)$$

being F the Faraday constant and I the current through the cell.

To provide a more fundamental electrochemical perspective, the lithium recovery capacity is not only reported in terms of mass (SAC, mg/g) but also as the lithium molar insertion fraction (y). This metric represents the moles of Li^+ intercalated per mol of LMO (LiMn_2O_4) and is calculated from the SAC using the respective molar masses of Li and LMO (M_{Li} and M_{LMO} , respectively):

$$y = SAC \times 10^{-3} \frac{M_{\text{LiMnO}}}{M_{\text{Li}}} \quad (4)$$

Expressing the Li content in terms of molar composition clarifies the specific electrochemical mechanism governing the electrosorption process. Note that if y is below 1, Li is inserted in tetrahedral sites, corresponding to the so-called 4V process, which retains the crystal structure of LMO. In contrast, $y > 1$ would force the lithium ions partially into octahedral sites, producing Jahn-Teller distortions and degrading the crystal structure.^{83,84} For the sake of clarity and to facilitate comparison with theoretical limits, all SAC values reported



hereafter are accompanied by their corresponding lithium molar insertion fraction (γ) in parentheses.

Experiments performed at a cell voltage of 0.4 V, presented in **Figure 2A**, show negligible differences between the deionization of LiCl and LiCl/NaCl mixture solutions. This is expected because the applied voltage is insufficient to significantly activate the intercalation of Li⁺ in the LMO electrode, with the maximum SAC values being (7.2±0.1) mg/g (0.1876±0.0026). In contrast, at a cell voltage of 0.9 V (**Figure 2B**), oxidation of the LMO is anticipated, facilitating the intercalation of Li⁺ into its structure. As shown in the Figure, the system demonstrates considerable extraction capacity for Li⁺ in pure solution, reaching SAC values of (21.9±0.1) mg/g (0.5706±0.0026), with near-maximum efficiencies (**Table 1**). For a mixed solution, a less pronounced electrosorption curve, lower than that of LiCl, is observed.

Finally, to evaluate whether increasing the cell voltage enhances the selectivity of the process or induces side effects like undesired oxidation, additional experiments were conducted at 1.2 V. As shown in **Figure 2C**, the application of this cell voltage reveals a complex deionization behavior that, to our knowledge, has not been previously reported. One might expect that in a mixed solution containing both Li⁺ and Na⁺, the LMO electrode would only capture the Li⁺, remaining indifferent to the Na⁺. Conductivity measurements demonstrate that a desorption phenomenon occurs even during the ion-capture step in mixed solutions. This suggests that the elevated cell voltage not only intensifies the intercalation of Li⁺ into the LMO but could also be causing the desorption of previously adsorbed Na⁺, which is likely to be expelled from the electrode because of the preferential sorption of Li⁺. To confirm this hypothesis, we carried out real-time ICP-OES measurements of ion concentration using a 5 mM NaCl + 5 mM LiCl mixed solution (*Supplementary Information, Figure S5*). Initial absorption occurs at a similar rate for both Na⁺ and Li⁺ ions;



however, Na⁺ ion electrosorption is found to be much less sustained, and a net ion release is observed at the end of the process. Conversely, Li⁺ incorporation into LMO continues throughout the electrosorption step. Obviously, ion replacement occurs when Li⁺ is intercalated into the LMO lattice, causing the desorption of previously absorbed Na⁺.

3.3. Polymeric coating on LMO

During the cell operation, LMO experiences manganese dissolution into the aqueous electrolyte, resulting in the gradual degradation of the active material. This process becomes particularly significant in environments involving electrochemical potential variations, such as those present in the desalination cycles investigated. Several factors, including the pH of the electrolyte, the operating temperature, and the applied charge/discharge cycles, govern the extent of Mn dissolution. Such effects compromise the durability of LMO and restrict its applicability in long-life systems^{25, 85-88}. To address this limitation, several strategies have been proposed, notably structural modification through metal doping⁸⁹⁻⁹¹ to stabilize its spinel structure.

On the one hand, coating LMO with polymers has been posited as an effective strategy to enhance its stability^{86, 92}. This polymeric coating functions as a physical barrier, thereby mitigating the structural degradation of LMO caused by manganese dissolution in aqueous media. On the other hand, PSS coating AC enhances the electrical conductivity in proximity to the interfaces, thereby increasing cation uptake efficiency while impeding the co-ion penetration into the electrode during reverse-voltage operation⁴⁴⁻⁴⁷. For this reason, LMO has been combined with PSS, and a direct comparison between the LMO-soft electrode and its uncoated version is presented in **Figure 2**, where the experiments were repeated for the three different cell voltages with PSS-coated LMO (LMO-soft). It yields electrosorption-



desorption profiles (**Figure 2D-F**) for both the pure and mixed solutions that are qualitatively similar to those obtained with bare LMO (**Figure 2A-C**). Consequently, 1.2 V was designated as the operating cell voltage for all subsequent analyses of electrosorption and Li⁺/Na⁺ selectivity.

The concentration profiles are depicted in **Figure 3**. These measurements were taken for a 1.2 V cell voltage; the desorption was performed in RV mode. Polyelectrolyte-coated electrodes exhibit a more distinct conductivity minimum that occurs slightly earlier than in uncoated LMO. Subsequent to this minimum, there is a more rapid return of the conductivity to the inlet value. Despite a faster electrosorption, this phenomenon results in a lower overall uptake capacity compared to uncoated electrodes. **Table 1** shows that the SAC decreases from (44.5±0.1) mg/g (1.1593±0.0026) for the uncoated electrode to (34.1±0.1) mg/g (0.8884±0.0026) for the LMO-soft electrode, while the charge efficiency decreases from 0.91±0.02 to 0.76±0.02. For the uncoated LMO at 1.2 V, the molar insertion fraction exceeds the theoretical maximum of the 4 V plateau ($y > 1$). This over-lithiation explains the complex deionization behavior observed at this elevated voltage. In contrast, the LMO-soft electrode under identical conditions remains in the stable 4 V region, suggesting an interesting effect of the polyelectrolyte coating, even if the amount of retained Li⁺ (SAC) is slightly reduced.

When a cell voltage of 0.9 V or 0.4 V is applied, the insertion coefficient y remains below 1 for both electrode configurations, with SAC values lower for LMO-soft than for LMO electrodes. In the case of 0.4 V, SAC increases slightly when using LMO-soft electrodes, although it remains much lower than when higher cell voltages are applied. These differences indicate that the polymer coating facilitates the initial accessibility of Li⁺ ions to the active LMO substrate, attributed to the negatively charged sulfonate groups in PSS⁹³.



However, this phenomenon also hinders the subsequent intercalation of Li⁺ ions, resulting in diminished retention and accelerated, thus less prolonged, uptake kinetics. In mixed solutions (**Figure 3B**), a similar trend is observed for both electrode configurations. Initial sorption and subsequent desorption (minimum and maximum in conductivity, respectively, when 1.2 V applied) are accentuated in the case of LMO-soft, consistent with observations in pure solutions.

Considering the differences in ion affinity between AC and LMO, it is expected that the ratio of LMO to AC will be crucial for selectively capturing cations. This becomes particularly important in the desalination of LiCl or LiCl/NaCl solutions. Results for the AC:LMO-soft electrodes show that the amount of Li⁺ removed decreases as the ratio AC:LMO-soft is raised (**Figure 3C**). This confirms that the LMO component plays a relevant role in Li⁺ uptake, indicating that intercalation is more favorable than capacitive electrosorption within AC. Conductivity measurements in LiCl/NaCl mixed solutions often display a secondary maximum after the initial minimum (**Figure 2C,F**), attributable to Na⁺ desorption and specifically associated with the properties of the LMO component (**Figure 3D**).

Although the spinel framework is capable of accommodating Na⁺ ions, as previously reported for non-aqueous sodium cells⁹⁴, this process induces significant lattice strain. It triggers a phase transition where the original spinel structure partially converts into a layered phase (Na₂MnO₂). In our aqueous mixed system, the high thermodynamic preference of the LMO structure for Li⁺ ions leads to the rapid and competitive displacement of any transiently inserted Na⁺, thereby preserving the spinel framework. This ion-exchange-like mechanism results in the observed Na⁺ release shortly after the beginning of the uptake stage, manifesting as a secondary conductivity maximum (*Supplementary Information, Figure S5*). When the AC fraction exceeds 40:60 (AC:LMO), this maximum disappears,



demonstrating that AC contributes only through a non-selective capacitive process, where both Na⁺ and Li⁺ ions participate in building the EDLs within the carbon pores.

3.4. Tuning the desorption stage for cation selectivity

In electrochemical systems based on LMO, selectivity is influenced by the preferential intercalation capacity of lithium in the material structure, which favors the electrosorption of Li⁺ over Na⁺. In addition, the desorption of these ions may also exhibit selective behavior. To investigate this phenomenon, salt desorption was performed in two stages. In the first stage, the short-circuit mode (zero-cell voltage, ZV) was used. This is intended to allow ions less strongly bound to the electrodes to migrate out of them so that in this step, Na⁺ or just adsorbed (not intercalated) Li⁺ will be released into the solution. This observation is consistent with previous studies showing that Na⁺ preferentially adsorbs at the electrode surface without significant intercalation, whereas Li⁺ is more prone to intercalate into the LMO lattice ⁷⁸.

Measurements were performed with LMO and LMO-soft electrodes bathed in a LiCl and NaCl mixed solution (**Figure 4A-D**). Samples were taken for ion chromatography analysis at different times during the cycle to identify the ionic species present in the effluent solution at each step of the process. During the uptake phase (steps 1-2), Na⁺ and Li⁺ exhibit distinct behaviors: after approximately 50 s (step 2), Na⁺ is partially released while Li⁺ remains retained within the electrode (**Figure 4A-C**). Meanwhile, Cl⁻ continues to adsorb on both electrode types. In the subsequent zero-voltage desorption (step 3, ~330 s), both cations are released in small and nearly equal amounts (~ 0.15 mM each), regardless of whether LMO or LMO-soft electrodes are used (**Figure 4B,D**).



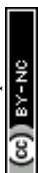
During the reverse-voltage stage (step 4), a stronger desorption of Li^+ occurs (0.62 mM for LMO and 0.52 mM for LMO-soft). In comparison, Na^+ desorption remains limited (0.21 mM for LMO) and within the experimental uncertainty for LMO-soft, consistent with the absence of residual Na^+ in the electrode. This stage also causes a higher conductivity increase, confirming that it is primarily associated with Li^+ release from the LMO structure, with minimal Na^+ contribution.

A transient Na^+ desorption is detected during the early uptake stages (steps 1-2), which reduces the amount of Na^+ captured for subsequent desorption. However, small residual amounts of Na^+ are still measurable after steps 3 and 4 for bare LMO. In contrast, the contribution of Na^+ during desorption is almost negligible for LMO-soft electrodes.

In this context, differential desorption of Na^+ and Li^+ is a key factor. During the initial ZV desorption step, Na^+ is preferentially released, whereas Li^+ remains bound due to its stronger interaction with the LMO lattice, consistent with our observations in mixed LiCl/NaCl solutions. When the cell voltage is reversed in the second step, Li^+ desorption becomes predominant. This differential behavior suggests that the polymer coating not only protects the electrode material but also enhances selectivity during desorption by favoring Li^+ -release over Na^+ -release.

3.5. Performance of LMO electrodes with asymmetric Li^+/Na^+ solutions

To evaluate the performance of the LMO and LMO-soft electrodes when employed under highly asymmetric conditions that closely resemble the challenges associated with lithium recovery, the experiments were conducted using a LiCl/NaCl mixture with a composition of 0.5 mM Li^+ + 9.5 mM Na^+ . This composition represents laboratory simulations designed to



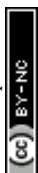
mimic the low lithium fractions typically encountered in natural brines, where the proportion of Li^+ in the total salt content varies between 0.1% and 2%⁹.

The corresponding results are shown in **Figure 5** as relative concentration changes (instead of absolute differences) for improving data visualization. Compared with the results in **Figure 4**, LMO-soft electrodes consistently remove about 6% of Li^+ during step 1 across all initial concentrations (**Figure 5C**), suggesting that the LMO-soft electrode architecture preserves its effectiveness for Li^+ separation, even under the highly asymmetric initial conditions. In contrast, bare LMO captures a negligible amount of Li^+ . The response of the system to Na^+ is similar in both cases, with an initial electrosorption followed by a pronounced release (**Figures 4-5**).

4. Conclusions

This study delves into the use of LMO as a promising active electrode material for selective lithium recovery in hybrid electrochemical ion separation cells, and its combination with polyelectrolyte layer (LMO-soft electrodes). By exploiting the intrinsic intercalation capabilities of the spinel lattice, LMO successfully overcomes a significant constraint of conventional capacitive deionization using AC electrodes: the incapacity to differentiate between monovalent cations.

Voltage-dependent experiments confirmed that Li^+ uptake increases markedly with applied potential, reaching >40 mg/g at 1.2 V with efficiencies above 90%. We have found a non-expected behavior: the intercalation of Li^+ drives the desorption of Na^+ , which initially migrated to the LMO electrode, thereby unveiling a replacement mechanism that directly addresses the challenge of selectivity in mixed-ion environments. The adjustment of electrode composition led to a reinforcement of the interplay between capacitive adsorption



associated with AC and intercalation mechanisms relative to LMO. Concurrently, low levels

View Article Online
DOI: 10.1039/D6YA00009F

of activated carbon to lithium manganese oxide (AC:LMO) ratios have been observed to preserve Li⁺ intercalation and the associated Na⁺ displacement.

Moreover, a side result we have found by using combined conductivity and ion chromatography measurements is a sequential release, whereby Na⁺ is expelled during zero-voltage step and Li⁺ during reverse-voltage operation.

The introduction of a polyelectrolyte achieves a dual enhancement in electrode stability and ion separation. While LMO-soft demonstrated diminished uptake capacities, the coating effectively increases long-term durability and reshapes desorption profiles. Notably, these behaviors persisted under asymmetric feed compositions (0.5 mM Li⁺ + 9.5 mM Na⁺), selected as a laboratory simulation for the low-lithium conditions characteristic of brines. Despite the challenging conditions, LMO-soft electrodes demonstrated a consistent ability to recover Li⁺ while facilitating Na⁺ release. This finding underscores the robustness of the intercalation-desorption sequence when Li⁺ is present as a minor component within the salt mixture. This finding directly addresses the practical motivation of developing systems suited for realistic brine environments.

Overall, the results demonstrate the efficacy of combining intercalation-type electrodes with functional polymer coatings to create a versatile platform for selective lithium extraction. The study establishes a linkage between fundamental electrochemical mechanisms and the pressing need for sustainable alternatives to conventional lithium extraction. This connection is achieved by integrating voltage-driven intercalation, ion replacement, polymer-modulated desorption, and compositional tuning. This integrated approach delineates a pathway toward stable, efficient, and scalable electrochemical technologies for lithium recovery from saline resources.



View Article Online
DOI: 10.1039/D6YA00009F

Open Access Article. Published on 27 April 2026. Downloaded on 4/28/2026 1:30:01 AM.
This article is licensed under a Creative Commons Attribution-NonCommercial 3.0 Unported Licence.



Data availability

All the data, including raw data, will be shared via the Open Science Framework at Digibug at <https://digibug.ugr.es/handle/10481/25025>.

Conflicts of Interest

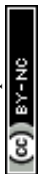
There are no conflicts to declare.

Acknowledgments

Financial support of this investigation by the grant PID2023-151881OB-I00 (AEI/10.13039/501100011033/ Unión Europea Next Generation EU/PRTR) is gratefully acknowledged. J.A.L.P. acknowledges FPU2023 (ref. FPU23/03086) funding by MICIU (España). We acknowledge support for the eLiFlow project by the European Union from the European Regional Development Fund (EFRE) and the State of Saarland, Germany.

Author contributions

S. Orozco-Barrera: Investigation, Data curation. J.A. Lirio-Piñar: Investigation, Data curation. C. Kök: Data curation, Writing-review & editing. G.R. Iglesias: Supervision, Methodology, Writing - review & editing. A.V. Delgado: Methodology, Writing - review & editing. V. Presser: Supervision, Methodology, Writing - review & editing. S. Ahualli: Supervision, Methodology, Writing - review & editing.



References

View Article Online
DOI: 10.1039/D6YA00009F

1. L. Kavanagh, J. Keohane, G. Cabellos, A. Lloyd and J. Cleary, *Resources-Basel*, 2018, **7**, 57.
2. C. Tabein, J. Dallas, S. Casanova, T. Pelech, G. Bournival, S. Saydam and I. Canbulat, *Minerals Engineering*, 2021, **163**, 106743.
3. W. Chen, J. Liang, Z. Yang and G. Li, *Innovative Solutions for Energy Transitions*, 2019, **158**, 4363-4368.
4. X. Zhang, A. Han and Y. Yang, *Journal of Materials Chemistry A*, 2020, **8**, 22455-22466.
5. P. Choubey, M. Kim, R. Srivastava, J. Lee and J. Lee, *Minerals Engineering*, 2016, **89**, 119-137.
6. P. Meshram, B. Pandey and T. Mankhand, *Hydrometallurgy*, 2014, **150**, 192-208.
7. P. Ji, Z. Ji, Q. Chen, J. Liu, Y. Zhao, S. Wang, F. Li and J. Yuan, *Separation and Purification Technology*, 2018, **207**, 1-11.
8. F. Brandt and R. Haus, *Minerals Engineering*, 2010, **23**, 659-661.
9. M. Vera, W. Torres, C. Galli, A. Chagnes and V. Flexer, *Nature Reviews Earth & Environment*, 2023, **4**, 149-165.
10. Y. Zhang, Y. Hu, L. Wang and W. Sun, *Minerals Engineering*, 2019, **139**, 105868.
11. M. Floyd, Master of Science Thesis, Utrecht University, 2021.
12. J. R. Rumble, *CRC Handbook of Chemistry and Physics*, CRC press Boca Raton, FL, 102 edn., 2017.
13. F. R. Spellman, *The science of lithium*, CRC Press, 2023.
14. D. Torres, K. Pérez, F. Galleguillos Madrid, W. Leiva, E. Gálvez, E. Salinas-Rodríguez, S. Gallegos, I. Jamett, J. Castillo, M. Saldana and N. Toro, *Metals*, 2024, **14**, 1095.
15. S. Mousavinezhad, S. Nili, A. Fahimi and E. Vahidi, *Resources Conservation and Recycling*, 2024, **205**, 107583.
16. M. A. Alkhadra, X. Su, M. E. Suss, H. Tian, E. N. Guyes, A. N. Shocron, K. M. Conforti, J. P. de Souza, N. Kim, M. Tedesco, K. Khoiruddin, I. G. Wenten, J. G. Santiago, T. A. Hatton and M. Z. Bazant, *Chemical Reviews*, 2022, **122**, 13547-13635.
17. P. Srimuk, X. Su, J. Yoon, D. Aurbach and V. Presser, *Nature Reviews Materials*, 2020, **5**, 517-538.
18. C. Kök, L. Wang, J. Ruthes, A. Quade, M. Suss and V. Presser, *Energy & Environmental Materials*, 2024, **7**, 517-538.
19. S. Porada, R. Zhao, A. van der Wal, V. Presser and P. M. Biesheuvel, *Progress in Materials Science*, 2013, **58**, 1388-1442.
20. P. M. Biesheuvel, H. V. M. Hamelers and M. E. Suss, *Colloid and Interface Science Communications*, 2015, **9**, 1-5.
21. B. P. Jia and W. Zhang, *Nanoscale Research Letters*, 2016, **11**, 64.
22. J. Oladunni, J. H. Zain, A. Hai, F. Banat, G. Bharath and E. Alhseinat, *Separation and Purification Technology*, 2018, **207**, 291-320.
23. A. Khalil, S. Mohammed, R. Hashaikh and N. Hilal, *Desalination*, 2022, **528**, 115611.
24. J. Farahbakhsh, F. Arshadi, Z. Mofidi, M. Mohseni-Dargah, C. Kök, M. Assefi, A. Soozanipour, M. Zargar, M. Asadnia, Y. Boroumand, V. Presser and A. Razmjou, *Desalination*, 2024, **575**, 117249.
25. A. Siekierka, M. Bryjak, A. Razmjou, W. Kujawski, A. Nikoloski and L. Dumée, *Membranes*, 2022, **12**, 343.
26. L. Wang, K. Frisella, P. Srimuk, O. Janka, G. Kickelbick and V. Presser, *Sustainable Energy & Fuels*, 2021, **5**, 3124-3133.
27. S. Arnold, L. Wang, R. Mertens, S. Wiczorek and V. Presser, *Separation and Purification Technology*, 2025, **367**, 132770.
28. S. Kim, J. Lee, J. S. Kang, K. Jo, Y. E. Sung and J. Yoon, *Chemosphere*, 2015, **125**, 50-56.



29. R. Trócoli, C. Erinmwingbovo and F. La Mantia, *Chemelectrochem*, 2017, **4**, 143-149. Article Online DOI: 10.1039/D6YA00009F
30. D. Weng, H. Duan, Y. Hou, J. Huo, L. Chen, F. Zhang and J. Wang, *Progress in Natural Science-Materials International*, 2020, **30**, 139-152.
31. T. Zhang, D. Li, Z. Tao and J. Chen, *Progress in Natural Science-Materials International*, 2013, **23**, 256-272.
32. R. Pitchai, V. Thavasi, S. Mhaisalkar and S. Ramakrishna, *Journal of Materials Chemistry*, 2011, **21**, 11040-11051.
33. A. Hashem, S. Abbas, X. Hou, A. Eid and A. Abdel-Ghany, *Heliyon*, 2019, **5**, e02027.
34. T. Eriksson, *Acta Universitatis Upsaliensis*, 2001.
35. K. Nakajima, F. Souza, A. Freitas, A. Thron and R. Castro, *Chemistry of Materials*, 2021, **33**, 3915-3925.
36. S. Ahualli, S. Orozco-Barrera, M. D. Fernandez, A. V. Delgado and G. R. Iglesias, *Polymers*, 2019, **11**.
37. L. Wang, Y. Liang and L. Zhang, *Environmental Science & Technology*, 2020, **54**, 5874-5883.
38. J. A. Lirio-Piñar, J. Calvo and S. Ahualli, *Physical Review E*, 2024, **110**, 034610.
39. P. A. Fritz, R. M. Boom and K. Schroen, *Separation and Purification Technology*, 2019, **220**, 145-151.
40. S. Ahualli, G. R. Iglesias, M. M. Fernandez, M. L. Jimenez and A. V. Delgado, *Environmental Science & Technology*, 2017, **51**, 5326-5333.
41. G. R. Iglesias, S. Ahualli, M. M. Fernandez, M. L. Jimenez and A. V. Delgado, *Environmental Science-Water Research & Technology*, 2019, **5**, 873-883.
42. G. R. Iglesias, S. Ahualli, A. V. Delgado, P. M. Arenas-Fernández and M. M. Fernández, *Journal of Power Sources*, 2020, **453**, 227840.
43. Y. Liu, Z. Li, X. Liu, Z. Chen, D. Fu, F. Fan, H. Xu and X. Wang, *Separation and Purification Technology*, 2025, **364**, 132343.
44. X. Gao, A. Omosebi, J. Landon and K. L. Liu, *Energy & Environmental Science*, 2015, **8**, 897-909.
45. X. Gao, A. Omosebi, N. Holubowitch, A. Liu, K. Ruh, J. Landon and K. Liu, *Desalination*, 2016, **399**, 16-20.
46. S. Ahualli, G. R. Iglesias and A. V. Delgado, in *Charge and Energy Storage in Electrical Double Layers*, Eds. S. Ahualli and A.V. Delgado, Elsevier, London, Chapter 9, 2018, 169-192.
47. K. Jo, Y. Baek, S. Kim, S. Hong and J. Yoon, *Korean Journal of Chemical Engineering*, 2020, **37**, 1199-1205.
48. Z. Li, Y. You, Z. Zhu, L. Wang, S. Ou, J. Xu and M. Yuan, *Applied Surface Science*, 2025, **682**, 161689.
49. T. Liu, A. Dai, J. Lu, Y. Yuan, Y. Xiao, L. Yu, M. Li, J. Gim, L. Ma, J. Liu, C. Zhan, L. Li, J. Zheng, Y. Ren, T. Wu, R. Shahbazian-Yassar, J. Wen, F. Pan and K. Amine, *Nature Communications*, 2019, **10**, 4721.
50. S. Brunauer, L. Deming, W. Deming and E. Teller, *Journal of the American Chemical Society*, 1940, **62**, 1723-1732.
51. D. Siderius, J. Evans, P. Iacomi, L. Vanduyfhuys, V. Van Speybroeck, V. Bon and S. Kaskel, *Angewandte Chemie-International Edition*, 2025, **64**, e202513606.
52. M. Thommes, K. Kaneko, A. Neimark, J. Olivier, F. Rodriguez-Reinoso, J. Rouquerol and K. Sing, *Pure and Applied Chemistry*, 2015, **87**, 1051-1069.
53. S. Ahualli, S. Bermudez, F. Carrique, M. L. Jimenez and A. V. Delgado, *Polymers*, 2020, **12**, 2097.
54. S. Orozco-Barrera, K. Wakabayashi, T. Yoshii, H. Nishihara, G. Iglesias, A. Delgado and S. Ahualli, *Separation and Purification Technology*, 2025, **354**, 129314.
55. M. Torkamanzadeh, C. Kök, P. R. Burger, P. Ren, Y. Zhang, J. Lee, C. Kim and V. Presser, *Cell Reports Physical Science*, 2023, **4**, 101661.
56. J. Rouquerol, F. Rouquerol, P. Llewellyn, G. Maurin and K. Sing, *Adsorption by Powders and Porous Solids: Principles, Methodology and Applications*, Academic Press, Amsterdam, 2 edn., 2013.



57. H. Marsh and F. Rodríguez-Reinoso, in *Activated Carbon*, Elsevier, Oxford, Marsh, H. Rodríguez-Reinoso, F. edn., 2006, 322–365. Article Online
DOI: 10.1039/D6YA00009F
58. L. Wang, W. Ding and Y. Sun, *Materials Research Bulletin*, 2016, **83**, 230-249.
59. J. Stumme, O. Ashokkumar, S. Dillmann, R. Niestroj-Pahl and M. Ernst, *Membranes*, 2021, **11**, 106.
60. A. Bhat, E. Reale, M. del Cerro, K. Smith and R. Cusick, *Water Research X*, 2019, **3**, 100027.
61. A. Kalde, J. Kamp, E. Evdochenko, J. Linkhorst and M. Wessling, *Membranes*, 2021, **11**, 671.
62. T. Richardson, S. Wen, K. Striebel, P. Ross and E. Cairns, *Materials Research Bulletin*, 1997, **32**, 609-618.
63. Y. Wang, Y. Shen, Y. Zhang, B. Yue and C. Wu, *Journal of Macromolecular Science Part B-Physics*, 2006, **45**, 563-571.
64. K. Ali, H. Raza, M. Malik, S. Ibn Shamsah, R. Amna and A. Sarfraz, *Journal of New Materials For Electrochemical Systems*, 2020, **23**, 1-6.
65. H. G. Shurvell, in *Handbook of Vibrational Spectroscopy*, John Wiley & Sons, Ltd., Hoboken, 2006.
66. E. Jarek, Z. Krasinska-Krawet, T. Kruk, L. Lamch, S. Ronka, K. Wilk and P. Warszynski, *Colloids and Interfaces*, 2021, **5**, 3.
67. Z. Xu and P. Braterman, *Journal of Materials Chemistry*, 2003, **13**, 268-273.
68. X. Wang, G. Feng and M. Ge, *Journal of Materials Science*, 2017, **52**, 6917-6927.
69. D. Rana, J. Biswakarma and S. Lustig, *Acs Omega*, 2024, **9**, 38998-39003.
70. V. Siipola, T. Tamminen, A. Källi, R. Lahti, H. Romar, K. Rasa, R. Keskinen, J. Hyväluoma, M. Hannula and H. Wikberg, *Bioresources*, 2018, **13**, 5976-6002.
71. I. Janekarn, A. Hunt, Y. Ngernyen, S. Youngme and N. Supanchaiyamat, *Royal Society Open Science*, 2020, **7**, 200438.
72. J. Serafin, B. Dziejarski, O. Fonseca-Bermúdez, L. Giraldo, R. Sierra-Ramírez, M. Bonillo, G. Farid and J. Moreno-Piraján, *International Journal of Hydrogen Energy*, 2024, **86**, 662-676.
73. E. Salama, M. Samy, H. S. Hassan, S. Mohamed, K. Mensah and M. F. Elkady, *Environ Sci Pollut Res Int*, 2024, **31**, 44863-44884.
74. SpectraBase, Spectrum: PDADMAC (LdlrNETyCBW), <https://spectrabase.com/spectrum/LdlrNETyCBW>, (accessed 23 September 2025, 2025).
75. S. Jareansin, P. Sukaam and B. Kusktham, *Polymer Bulletin*, 2019, **76**, 4507-4520.
76. J. Chen, M. Liu, H. Liu, L. Ma, C. Gao, S. Zhu and S. Zhang, *Chemical Engineering Journal*, 2010, **159**, 247-256.
77. A. B. D. Nandiyanto, R. Oktiani and R. Ragadhita, *Indonesian Journal of Science and Technology*, 2019, **4**, 97–118.
78. F. Marchini, D. Rubi, M. del Pozo, F. Williams and E. Calvo, *Journal of Physical Chemistry C*, 2016, **120**, 15875-15883.
79. N. Kuwata, G. Hasegawa, D. Maeda, N. Ishigaki, T. Miyazaki and J. Kawamura, *Journal of Physical Chemistry C*, 2020, **124**, 22981-22992.
80. B. Xu and S. Meng, *Journal of Power Sources*, 2010, **195**, 4971-4976.
81. J. Zhang, J. Shen, T. Wang, C. Wei, Y. Ma, C. Zhu and Y. Yue, *Electrochemical Acta*, 2013, **111**, 691-697.
82. E. Kim, B. Kim and J. Lee, *Environmental Engineering Research*, 2024, **29**, 230677.
83. J. Goodenough and K.S. Park, *Journal of the American Chemical Society*, 2013, **135**, 1167-1176.
84. F. Yu, Y. Wang, C. Guo, H. Liu, W. Bao, J. Li, P. Zhang and F. Wang, *Crystals*, 2022, **12**, 317.
85. X. Zhu, F. Meng, Q. Zhang, L. Xue, H. Zhu, S. Lan, Q. Liu, J. Zhao, Y. Zhuang, Q. Guo, B. Liu, L. Gu, X. Lu, Y. Ren and H. Xia, *Nature Sustainability*, 2021, **4**, 392-401.
86. Z. I. Radzi, K. H. Arifin, M. Z. Kufian, V. Balakrishnan, S. R. S. Raihan, N. Abd Rahim and R. Subramaniam, *Journal of Electroanalytical Chemistry*, 2022, **920**, 116623.
87. G. Tan, S. Wan, J. Chen, H. Yu and Y. Yu, *Advanced Materials*, 2024, **36**, 2310657.



88. Q. Xia, X. Lei, F. Yue, W. Liu, C. Xu, J. Xu, M. Yang, X. Huang, D. Su and H. Xia, *Nano Letters*, 2025, **25**, 7892-7899. View Article Online
DOI: 10.1039/D6YA00009F
89. A. Siekierka, *Separation and Purification Technology*, 2020, **236**, 116234.
90. A. Siekierka, *Desalination*, 2022, **527**, 115569.
91. Y. Wu, P. Shi, Y. Zhong and R. Cai, *Energy & Fuels*, 2023, 4083-4093.
92. K. Lin, S. Yang, Z. Shi, Q. Fan, Z. Liu and L. Liu, *Journal of Power Sources*, 2022, **520**, 230768.
93. H. Liu, K. Chen, C. Fang and C. Chiu, *Electrochimica Acta*, 2021, **375**, 137915.
94. N. Yabuuchi, M. Yano, S. Kuze and S. Komaba, *Electrochimica Acta*, 2012, **82**, 296-301.



Figures

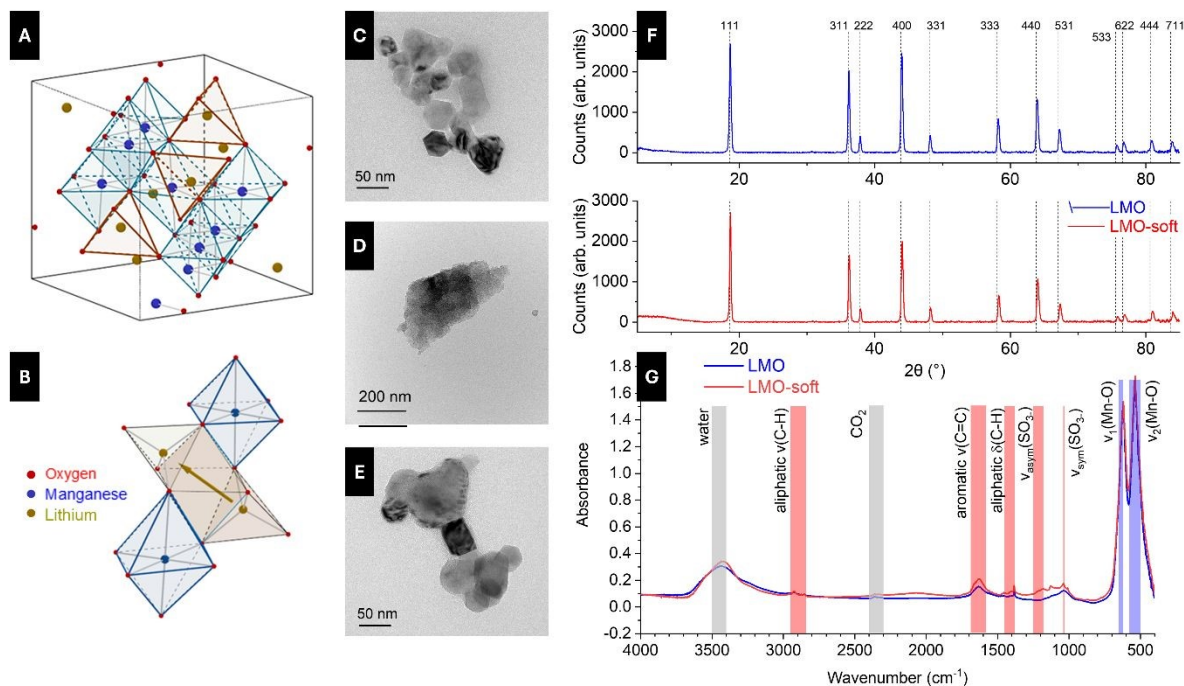
View Article Online
DOI: 10.1039/D6YA00009F

Figure 1. Structural and physicochemical characterization of electrode materials. (A) Crystal structure of spinel LiMn_2O_4 and (B) lithium diffusion pathways. Transmission electron micrographs of (C) LMO, (D) AC activated carbon, and (E) carbon black particles. (F) X-ray diffractograms of pristine and PSS-coated LMO; Miller indices in the top panel were obtained using PowderCell 2.4. (G) Fourier-Transform infrared spectra of LMO and PSS-functionalized LMO; grey bands correspond to environmental contaminants (H_2O , CO_2), red bands to PSS coating, and blue bands to LMO vibrations.



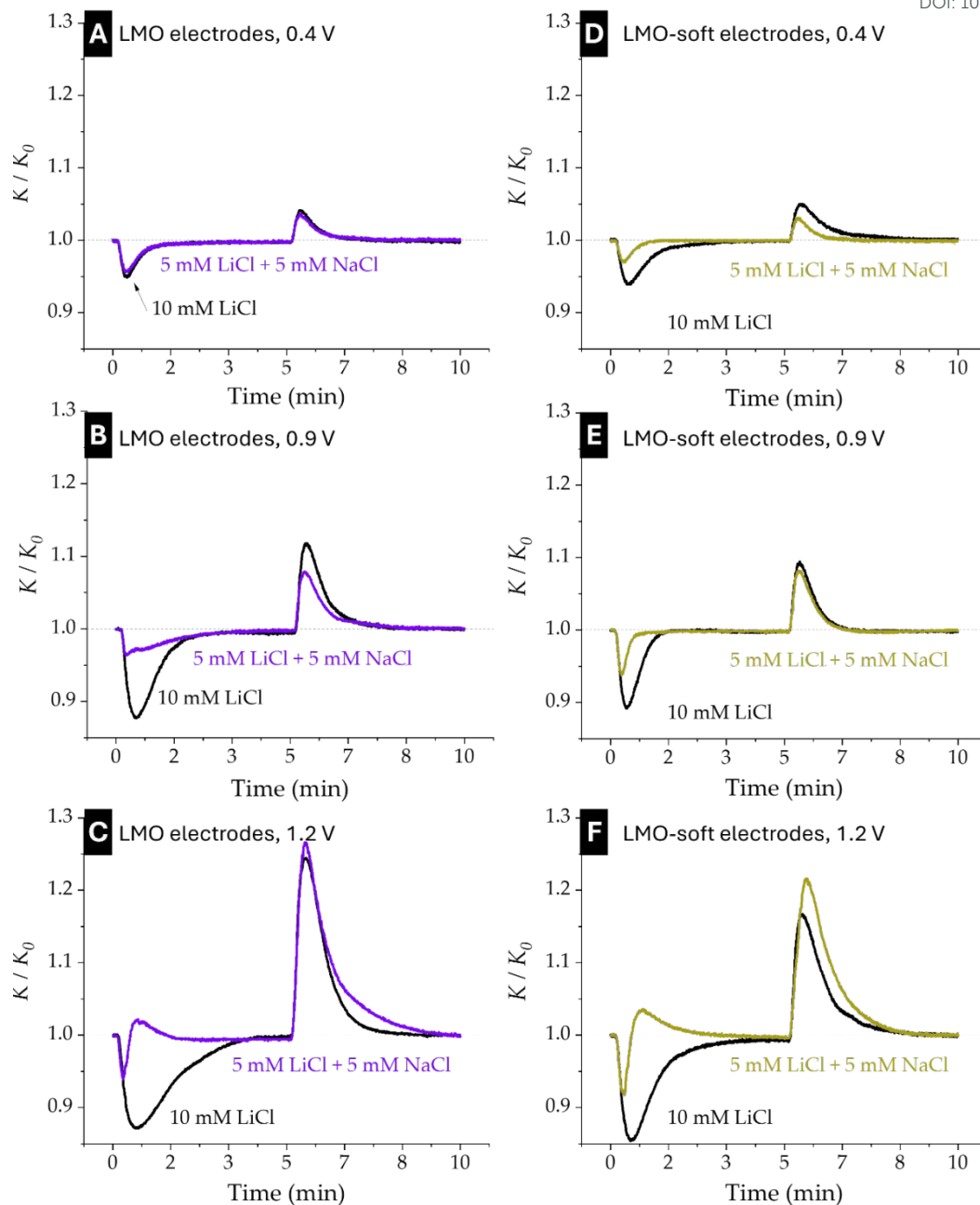
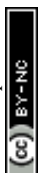


Figure 2. Relative conductivity (outlet/inlet) versus time during sorption-desorption cycles for two feed compositions: 10 mM LiCl and 5 mM NaCl + 5 mM LiCl. A-C: bare LMO electrodes operated at cell voltage of 0.4 V (A), 0.9 V (B), and 1.2 V (C) during the uptake stage (measured against an AC counter electrode). D-F: PSS-coated LMO electrodes operated at cell voltage of 0.4 V (D), 0.9 V (E), and 1.2 V (F) during the uptake stage. All cycles were done with RV desorption.



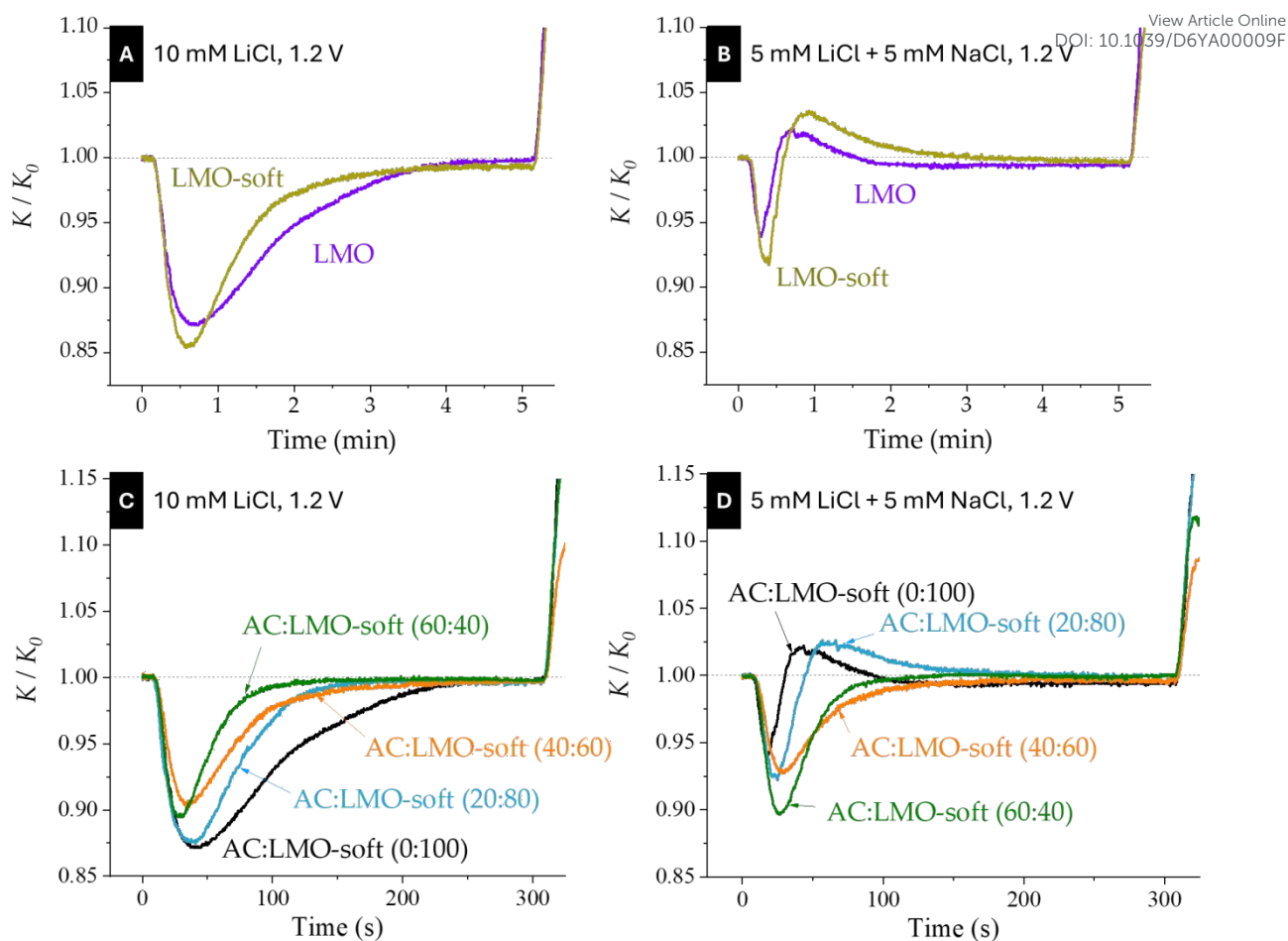


Figure 3. Relative conductivity (outlet/inlet) at 1.2 V cell voltage for LMO and LMO-soft electrodes. Panels (A) and (B) correspond to desalting of 10 mM LiCl and 5 mM LiCl + 5 mM NaCl solutions, respectively. Panels (C) and (D) show the uptake stage for the same solutions, for the indicated AC:LMO-soft electrode compositions.



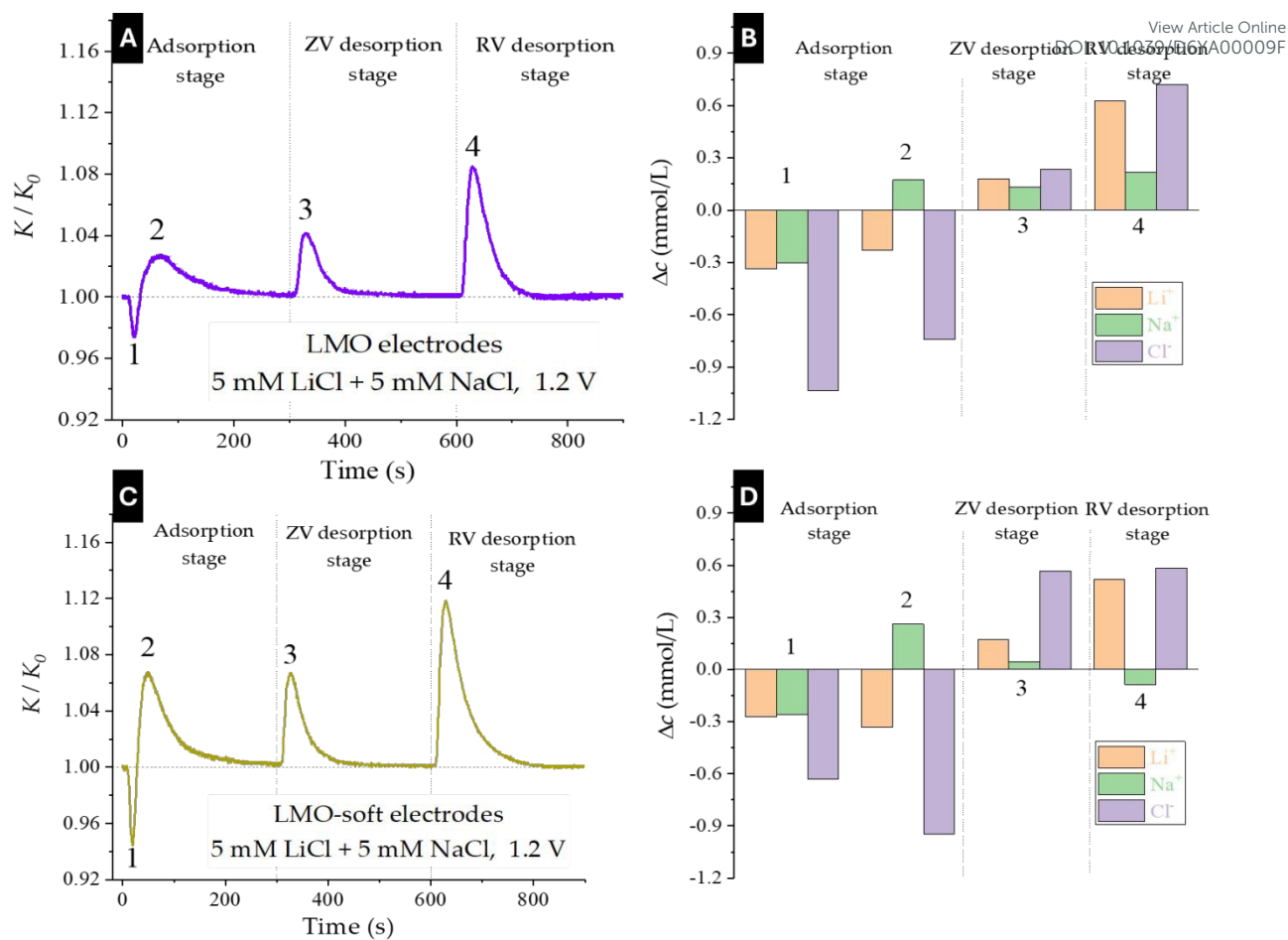
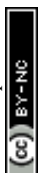


Figure 4. Performance data for LMO (A-B) and LMO-soft (C-D). Conductivity K of the outgoing solution relative to that of the incoming one, K_0 (A,C), and concentration increments (relative to those of the feed solution, 5 mM NaCl + 5 mM LiCl) (B,D) as a function of time. Successive desorption steps at short-circuit (Step 3) and reversed voltage (Step 4) for a 1.2 V cell voltage. The sampling times are 18 s (1), 60 s (2), 330 s (3), and 630 s (4).



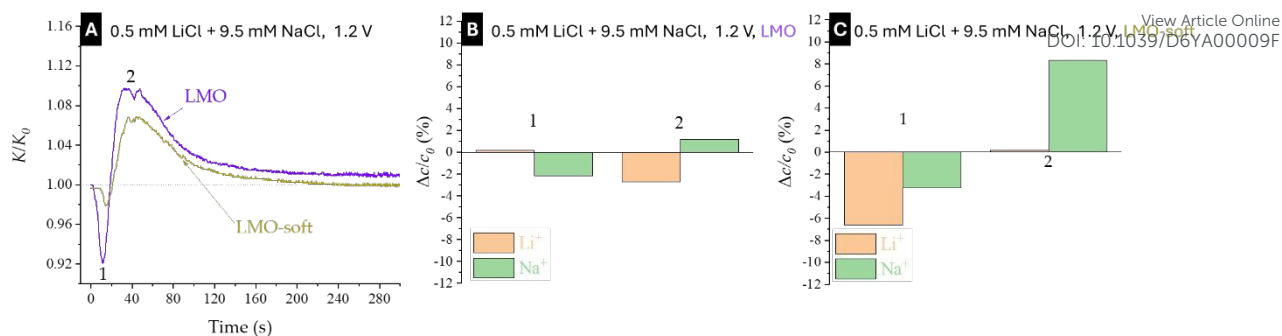
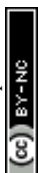


Figure 5. (A) Relative conductivity in the uptake stage when desalting a 0.5 mM LiCl + 9.5 mM NaCl mixed solution for electrodes with LMO and LMO-soft. Relative sodium and lithium concentration changes in steps 1 and 2 of Figure 5A for LMO (B) and LMO-soft (C) electrodes. The cell voltage was 1.2 V.



Table**Table 1.** Calculated SAC values and charge efficiency for measurements with 10 mM LiCl solutions and the cell voltage indicated.

	Solution	Cell voltage (V)	SAC (mg/g)	Lithium molar insertion fraction y	Charge efficiency ϵ
LMO electrode	10 mM LiCl	0.4	7.2±0.1	0.1876±0.0026	0.96±0.02
		0.9	21.9±0.1	0.5706±0.0026	0.94±0.02
		1.2	44.5±0.1	1.1594±0.0026	0.91±0.02
LMO-soft electrode	10 mM LiCl	0.4	10.7±0.1	0.2788±0.0026	0.81±0.02
		0.9	12.5±0.1	0.3257±0.0026	0.78±0.02
		1.2	34.1±0.1	0.8884±0.0026	0.76±0.02



Data availability

View Article Online
DOI: 10.1039/D6YA00009F

All the data, including raw data, will be shared via open science framework at Digibug at

<https://digibug.ugr.es/handle/10481/25025>.

